Nuclear Instruments and Methods in Physics Research B 560 (2025) 165626

Contents lists available at ScienceDirect

Nuclear Inst. and Methods in Physics Research, B

journal homepage: www.elsevier.com/locate/nimb

High-throughput MeV ion beam analysis – quantitative full stoichiometry imaging of a granite

S. Möller *, K.F. Muzakka, D. Höschen, M. Finsterbusch

Forschungszentrum Jülich GmbH, Institute of Energy Materials and Devices - Materials Synthesis and Processing, 52425 Jülich, Germany

ARTICLE INFO

Keywords:
Ion beam analysis
Material analysis
μ-PIXE
RBS
NRA
PIGE

ABSTRACT

MeV Ion-Beam analysis (IBA) can quantify the whole periodic table, provide tomographic information, analyse elements up to 100 μm depth, and achieve down to nm depth resolution under ideal conditions. This brings along a high degree of instrument and data analysis complexity. Only recently, optimised instrument geometry and precision on the hardware-side and artificial intelligence, modern computing power, and new nuclear cross-sections on the software-side enabled analysing the IBA spectra effectively and with only little human interaction. The increased throughput reinvents IBA as an elemental imaging technology.

This work presents a 5x5mm^2 imaging of a granite sample with 100x100 pixels using four IBA methods measured and analysed within 24 h. This demonstrates the capabilities of the newly developed software and hardware solutions. The analysis reveals SiO_2, an Al, and a Fe rich phases in the granite. The present elements and their concentrations match typical granite phases.

1. Introduction

Materials are a key component in any technological development and product, making material development and characterisation a key technology for many material inventions [1]. Analysis methods enable a quantitative picture of processes inside and the composition and purity of materials. Ion-Beam-Analysis (IBA) probes materials using scattering of MeV ions, typically H and He, with the sample atoms. IBA offers unique analytical possibilities through its sensitivity for the whole periodic table, including light elements such as lithium and hydrogen and its superior detection limits compared to electron or x-ray based local analysis methods [2]. The origin lies in the physics of bremsstrahlung and energy-loss differing strongly between ions, electrons, and photons and the MeV energy enabling access to nuclear information. IBA comprises several sub-methods each exploiting certain interaction products and physics. Among these sub-methods, Rutherford-Backscattering Spectrometry (RBS), Particle-Induced X-ray Emission analysis (PIXE), Nuclear-Reaction-Analysis (NRA), and Particle-Induced Gamma-ray Emission analysis (PIGE) represent a particularly powerful subset [3]. Fig. 1 presents the potential contributions of each sub-method to a stoichiometric IBA analysis, demonstrating an access to the whole periodic table by combining the four methods in a single measurement.

Analytical setups combine these four sub-methods for extending their analytical power [4]. State-of-the-art setups enable absolute quantification with statistical uncertainties down to ~ 1 % [5,6] and Limits-of-Detection (LoD) in the ppm range in many cases. The absolute uncertainty is usually limited by the required measured input data, in particular the stopping power and the reaction cross-sections. IBA is typically conducted in the form of a point analysis where a single point or a small set of points on selected locations on a sample are analysed. Mapping analysis adds lateral (2D) or even tomographic (3D) information requiring significantly more points and therefore measurement time. Typical IBA acquisition times of several minutes to hours per point and manual data evaluation prevent acquiring a point quantity suitable for producing images. Due to the easier interpretation, mapping is mostly related to PIXE, so-called μ-PIXE, missing out the light elements such as Boron or Lithium and the tomographic information. As demonstrated in Fig. 1, it is advantageous to include more IBA methods in the mapping analysis to access the whole periodic table. Numerous other methods enable access to the whole periodic table, some with even better detection limits, but the resulting combined information can suffer from inconsistencies. With IBA, even when combining several detectors, projectile species (H, He…), and projectile energies, the measurement is consistent by using the same detectors, physics, analysis location, input data, and a consistent data interpretation.

IBA mappings with resolutions in the order of 256x256 pixel [7,8]

* Corresponding author.
E-mail address: s.moeller@fz-juelich.de (S. Möller).

https://doi.org/10.1016/j.nimb.2025.165626
Received 18 October 2024; Received in revised form 22 December 2024; Accepted 13 January 2025
Available online 16 January 2025

using beam scanning limited the accessible area to about 2x2 mm^2 due to the scanning ranges. The application of beam scanning is very successful in scanning electron microscopy, but MeV ions require significantly stronger and thus larger beam optics, resulting in technical differences between IBA and electron microscopes. Furthermore, except for PIXE, IBA measurements require longer integration times due to the lower nuclear reaction cross-sections compared to electron microscopy methods. The limited counting statistics and the continuous movement limit the full stoichiometric analysis of the IBA spectra in the beam-scanning mode in particular for inhomogeneous samples. Moving the sample with a fixed beam resolves this limitation with up to 600x600 mm^2 analysis areas already demonstrated [9], but with significantly lower lateral resolution. In conclusion, a combination of RBS, NRA, PIXE, and PIGE with improvements of throughput and precision are desirable.

Besides these parameter range limitations, the limited application of IBA lies in the highly complex data interpretation, since the elemental depth profiles have to be extracted from complex spectra through physics models such as SimNRA [10] or NDF [11,p.]. Thousands or even millions of these spectra have to be fitted, each with about 10–50 free parameters in order to produce a high resolution 2D or 3D analysis. This limits throughput and made IBA useful only for a limited number of scientific applications implemented in specific IBA laboratories having the trained experts to interpret the data [12]. Advances in the setups, computing power, artificial intelligence, and IBA physics now enable solving these long-lasting difficulties [13–17]. Several groups pursue this increased integration of hardware and software into a multi-detector IBA tool, e.g. [18–20], which this work claims to continue. This reinvents IBA as a quantitative imaging method.

We demonstrate this claim through a 100x100-pixel IBA map of an unprocessed granite stone acquired and evaluated within 24 h by an automated hard- and software toolset. 30 years ago, geological sciences were already seen to profit from IBA [21] and later development confirmed this [8,22]. The developments presented here extend the analytical capabilities by a different sample manipulation approach and a powerful software exploiting more information available with IBA.

2. High-throughput IBA

A 1.7 MV tandem accelerator supported by a Duoplasmatron ion source supplies the proton beam of 2970 ± 20 keV and 7nA for IBA. The system and the ion optics are equipped with power supplies providing 10^{-5} stability in order to provide a long-term stable and high current–density beam. A triple quadrupole magnet with 9 mm bore and 100 mm magnet length is used for focussing the ion beam to a 50 μm quadratic spot size.

An Aachen Ion Beams BeamScience end-station [4] is used for IBA. It is equipped with a 300 μm and a 1500 μm Si-PIN detector at 150° reaction angle using an RC preamplifier, a KETEK SDD with 130 eV FWHM, transistor reset ASIC, and 125 μm Be window at 112.5°, and a Mirion HPGe detector at 0°. The data acquisition is synchronised to 5–10 ms differences in spectral acquisition time through the data acquisition software. The ion current is measured using a + 300 V bias applied to the isolated sample through a tri-axial wire connected to a Keithley 6485 A meter with an effective resolution of 10 pA. The fixed-beam geometry applied here results in a high freedom of choice for the manipulator. The installed sample manipulator can scan up to 50x50 mm^2 areas on the sample with a resolution of 10 nm. Besides the high-resolution manipulator used here, also larger scan areas or external beam analysis could be implemented. The devices control software synchronises the data acquisition of all detectors and the positioning and saves spectra and metadata. The IBA methods RBS, NRA, PIXE, and PIGE are combined in the analysis setup for spectrum acquisition synchronised to < 10 ms. Fig. 2 explains the data workflow. The measurement implements a discrete mapping algorithm with static beam and moving sample and an ion fluence condition ensuring a constant ion fluence for

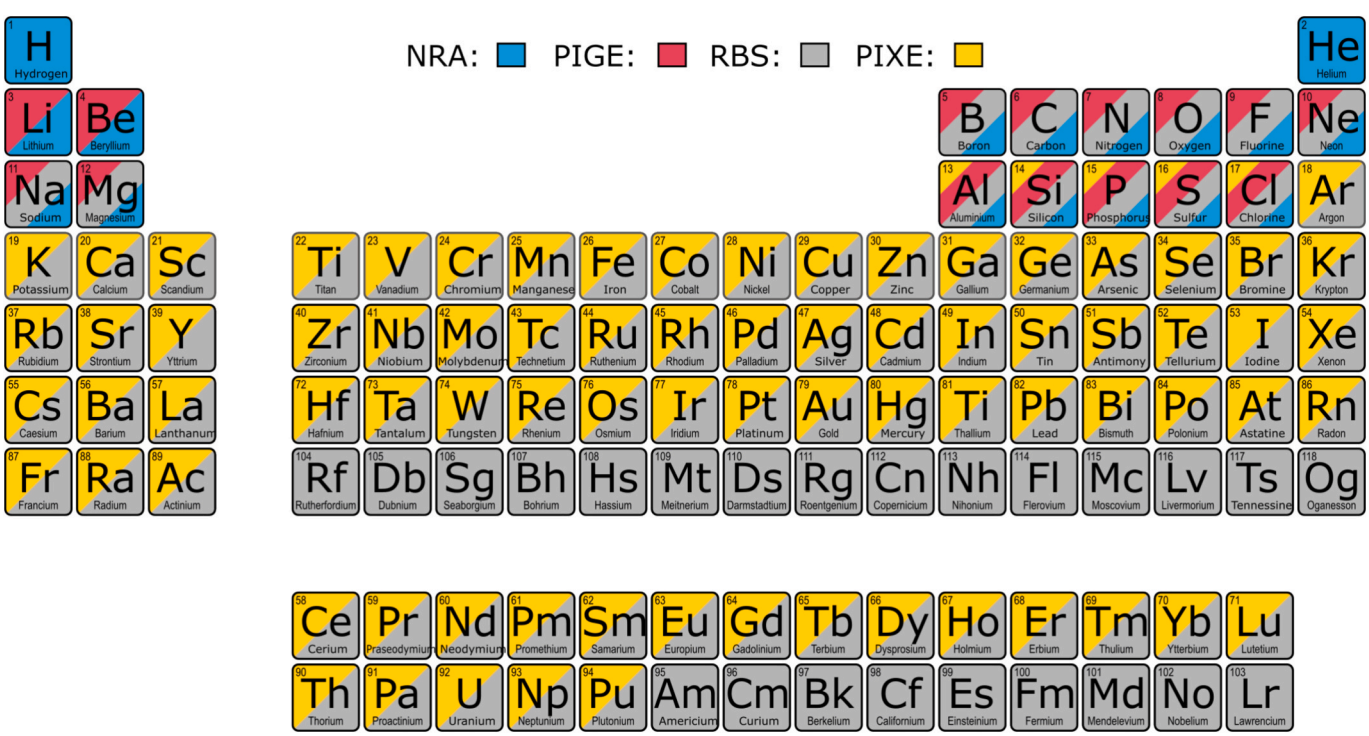

Fig. 1. The IBA periodic table indicates the analytical capabilities of each IBA sub-method. The exact limits of each sub-methods are subject to the implementation and technology of the end-station. Each sub-method is useful for certain elements, but no single method can cover the whole periodic table. Not all IBA methods are considered, e.g ERD is missing. Only ~ 5 elements can be analysed with all 4 sub-methods. The sensitivity also depends on the projectile species and energy not detailed here. From Ge upwards RBS cannot separate neighbouring elements anymore, limiting its analytical capabilities in materials containing neighbouring elements. H and He isotopes can be analysed using NRA, but the common isotope (^{1}H and ^{4}He) detection is limited.

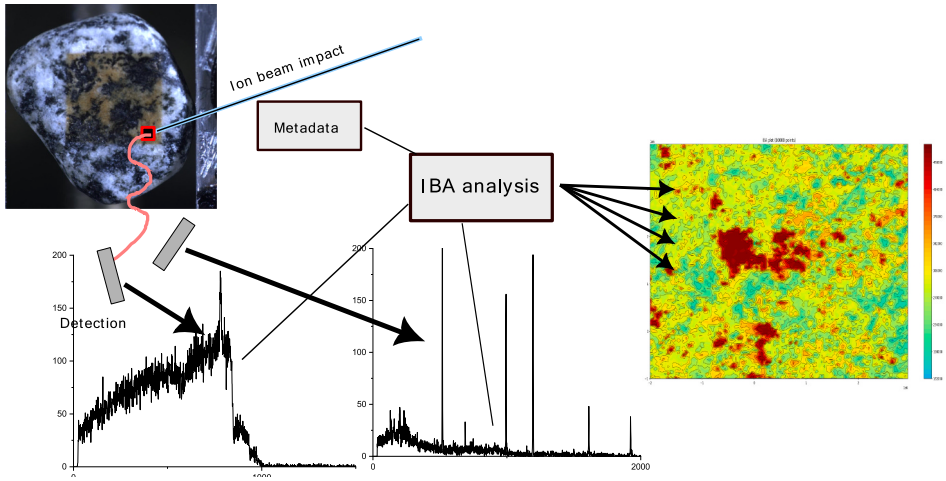

Fig. 2. Workflow of IBA. The pixels are obtained by moving the sample to a matrix of discrete positions. Each detector generates a spectrum (actual measured spectra are shown) for every pixel on the sample. These spectra, together with the metadata, are fed into the analysis software. The accumulated evaluations are combined to elemental sample maps.

every pixel. This approach avoids image plane distortions, since the sensors attached to the piezo motors provide the lateral coordinate.

Three software modules acquire, process, and display the IBA results. The PIXE data is processed using GUPIX3.03 [23], the PIGE, NRA, and RBS data using SimNRA 7.03 [10]. The AutoNRA software [13] operates these programs in a parallelized processing for batch interpretation of the 40,000 spectra plus 10,000 metadata files and adds additional fitting algorithms to SimNRA to find global and local minima more efficiently. The processing runs on a 64-core workstation PC with up to 1500 iterations per spectrum, requiring about the same 24 h as the data acquisition. AutoNRA requires the user to enter a reference composition of the approximate sample composition, which is derived from the peaks found in the IBA methods and a first manual SimNRA interpretation of a single data point. SimNRA is set to use the standard settings plus "multiple scattering" and electronic stopping power data using SRIM2013. Gupix is fitting using the "iterated matrix solution" with O as invisible element. The software loads all resulting elemental depth profiles and generates the plots presented below using a linear interpolation algorithm.

The sample is collected from regular gravel. After wiping with propanol, it is installed into the end station. Further sample preparation is not required, although this preparation represents drawbacks in terms of not removing weathering artefacts and not providing the ideal analysis geometry. The sample surface is not perfectly flat but its normal is oriented towards the incident beam by clamping it onto the backside of a slit holder made from aluminium. The samples irregular non-polished surface introduces additional uncertainties into the spectral evaluation. For the thick and in-depth homogeneous sample, the effect is small and relates to geometric differences in the particle energy loss for the varying impact angles of the projectiles. In the given case, SimNRA and Gupix analyses comparing impact angles from 0 to 20° reveal additional uncertainties of 3 % (RBS, NRA, PIGE) and 0.7 % (PIXE), respectively, introduced by the non-polished surface. Within 24 h of continuous measurement, a 5x5 mm^2 mapping with ~ 9 s = 70 nC per point is acquired. This corresponds to a map of 100x100 pixel with 50 μm analysis spots. The spectra contain about 20,000 counts for RBS, NRA, and PIGE and 500,000 counts for PIXE. The related total uncertainty in the elemental concentrations is 10 %. The raw data is published separately [24].

After IBA, the sample is checked for nuclear activation using a Berthold LB124 scintillation detector. No activity beyond the natural level is detected, allowing for handling of the analysed sample in regular laboratories. Most of the potential products from (p, n) reactions of the detected elements are short lived with half-lifes of minutes or less. These radioactive isotopes, if produced at all, will decay before the operator takes out the sample, hence cannot be detected. MeV protons can result in a few long-lived activation products such as Ca-41 (from K) or Co-56 (from Fe), but the reaction cross-sections are small at 3 MeV, not resulting in an activity above the detector LoD and the German free handling limit according to calculations similar to [25].

3. Results

Fig. 3 l) shows a photography of the sample after analysis. The sample is slightly affected by the ion impact, visible as a darkening of the white parts of the granite. This effect is often observed in (semi-) transparent materials and originates from lattice damage induced by the ion impact cascades. This structural damage cannot influence the IBA result, which relies only on the elemental composition.

The analysis yields signals above the LoD for 11 elements (C, O, Al, Si, Cl, K, Ca, Ti, Mn, Fe, Sr), displayed in Fig. 3 a) to k), with the lowest concentration found for Sr and Mn on the 500 ppm level. A search for Li (LoD = 1 %), F (LoD = 1 %), and B (LoD = 10 %) yields no presence of these elements according to the related NRA (α-emission) and PIGE (γ-lines) reactions. Consequently, PIGE provides only negative information in this case, which is also important. The information on C and O are related to the RBS analysis, while the heavier elements are mostly provided by PIXE due to its advantageous statistics compared to RBS. RBS shows flat depth profiles within the given limits. With the given 70 nC ion fluence, the lowest LoD is 14.8 ppm for Ti. H and He cannot be detected using the presented analysis, but besides these elements, the presented maps can be assumed to represent the full stoichiometry.

The comparison of the optical and elemental images reveals three major phases, a black Fe, Mn, Ti-rich, a white Si-rich phase, which ismu not darkened by the ion beam, and another white Al-rich phase. In most locations, a thin surface layer of mostly carbon is found with a thickness of up to $2.0*10^{22}$ atoms/m^2 and a median of $0.87*10^{22}$ at./m^2 thickness (Fig. 3h), corresponding to ~ 250 nm and 76 nm, respectively, assuming pure graphite. In the bulk, the C content ranges between 0 and 2.4 at.% with a median of 1.2 at.%, see Fig. 3i). The Si-rich part incorporates a higher average concentration of C compared to other regions. The optical image indicates the carbon is not present as pure graphite layer, which would be a grey colour impression, but rather as a surface near enrichment not resolved within the given depth resolution.

Trace amounts of Sr of up to 0.05 wt (weight) % are present in the Al rich phase, but no Sr is found in the Si and Fe rich parts. This suggest the Al rich phase is a plagioclase feldspar ($(Na,Ca)(Si,Al)_4O_8$) where Sr substitutes Ca atoms. In the Fe rich parts up to 11.2 wt% of Fe is found. Together with the presence of Al and Si this suggests a Biotite (K(Mg,Fe,

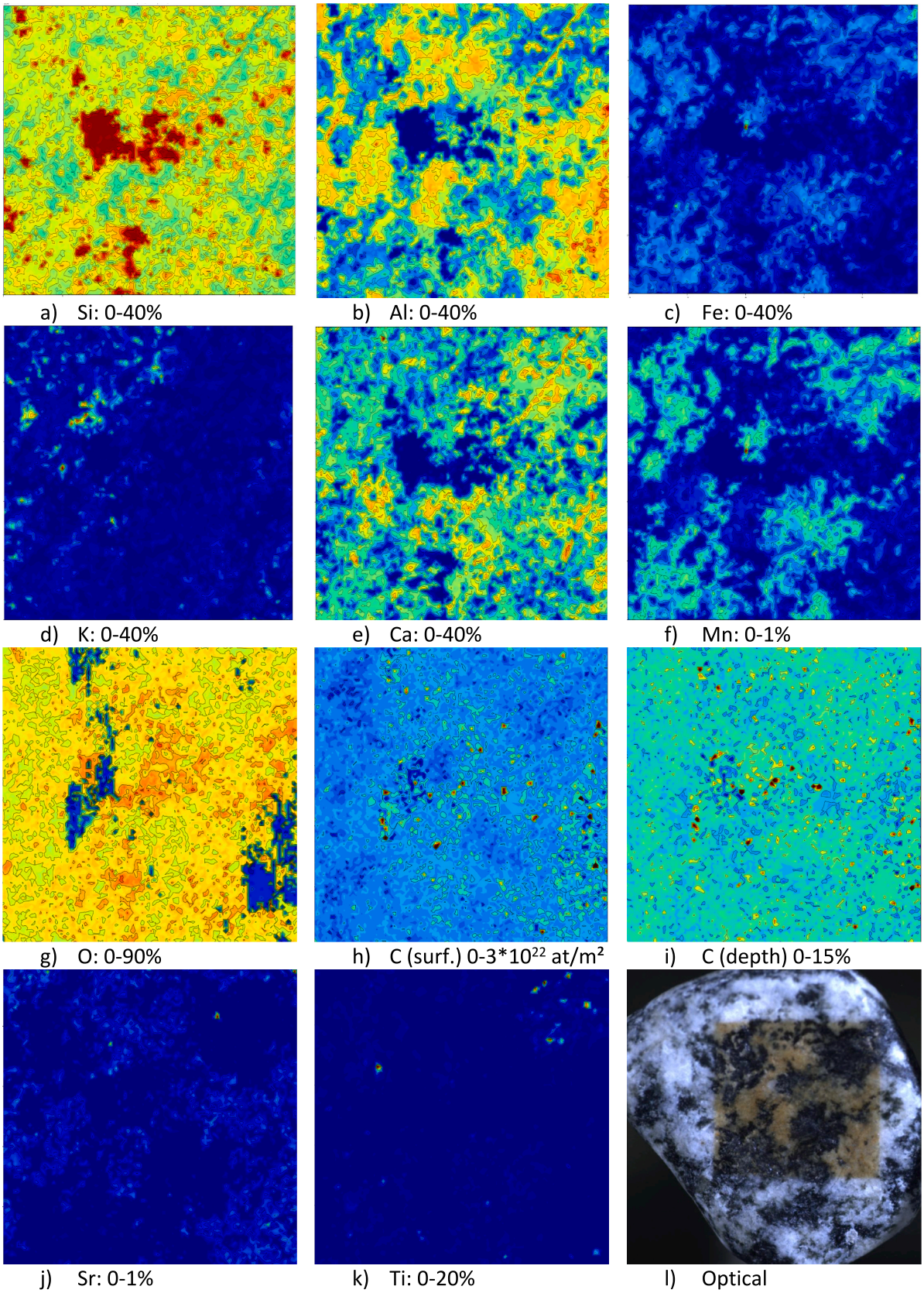

Fig. 3. Observation camera image (l) and 10.000 points elemental concentration mapping (a-k) results of the 5x5 mm^2 scan on the granite using IBA. The 5x5 mm^2 analysis region is clearly visible by a darkening of the white parts of the granite in the optical image. Black parts of the granite can be attributed to Fe, Mn, Ti rich and bright parts are either SiO_2 or Al rich compounds. Concentrations are on a linear scale of 0 (dark blue) to the given maximum percentage (dark red). (For interpretation of the references to colour in this figure legend, the reader is referred to the web version of this article.)

$Mn)_3(AlSi_3O_{10})(OH)_2$). The median over the whole area is at 3.4 wt%. Mn is highly correlated with Fe with up to 0.27 wt% Mn in the Fe rich parts and a median of 0.08 wt% over the whole area, supporting the Biotite assumption. Similarly to Mn, Ti is strongly correlated with Fe, but it is less evenly distributed. Most of the Ti is found in a few single data points reaching up to 13.5 wt% with a median over the whole surface area of only 0.08 wt%. This indicates minor inclusions of ilmenite ($FeTiO_3$). Ca is found in the Al and the Fe rich parts relatively evenly distributed with up to 20 wt% and a global median of 8.6 wt%. The Al rich phase contains up to 22.5 wt% Al with a global median of 11.6 wt%. The combination of Ca and Al weight percentages and the absence of Na clarifies the plagioclase feldspar as anorthite ($CaAl_2Si_2O_8$, with 19.4 wt% Al and 20 wt% Ca) dominated.

In the Si rich part, no Ca can be found. K reaches up to 8 wt% concentration with a median of 0.3 wt% and is a part of the Biotite mentioned above (Biotite nominal 8.4 wt% K content). Si reaches 46 wt % in the Si rich part, but is present in all phases with a median of 28.3 wt %. The weight percentage in the Si-rich phase fits perfectly to Quartz (SiO_2) with 46.7 wt% Si. Cl is uncorrelated to the other elements with a median concentration of 0.1 wt% and a maximum of 0.5 wt%.

Regarding the light elements, O is found mostly homogeneously distributed over the sample in concentrations of a median of 60.6 atomic % and a standard deviation of 2 atomic %. Parts of lower O concentrations (blue) are related to non-convergent fits. This problem typically affects < 1 % of the data points and can be excluded through a Z-score filtering. In the presumed SiO_2 rich part, higher concentrations of O = 65 % and Si = 32 % (=46 wt%) are found. This supports the assumption of pure SiO_2 regions with its nominal 33.3 % Si and 66.6 % O. Carbon is at a median concentration of 5.8 atomic % in the bulk, but statistical fluctuations due to limited counting statistics are significant for this element. In the SiO_2 regions, the C concentration is slightly below the average value.

4. Conclusions

The combined IBA using scattered ions, x-rays, and gamma rays provides a unique insight into the full material stoichiometry of the analysed sample. The presented IBA combines several smaller advances in software and hardware to a large advance of the technological level. The analysis identified 3 phases, SiO_2, a Fe-rich and an Al-rich phase. The composition and the detection limits are consistent with a full stoichiometric characterisation. Light elements such as Li, F, and B are not found.

The presented granite analysis demonstrates the strength of IBA elemental imaging. The sample features an intermediate complexity in terms of the number of elements (11 elements present in the sample) and the complexity of the elemental depth profiles (2 layers), which are found to be flat beyond a surface C layer. Yet the sample is a common sample type. The IBA is conducted without any preparatory steps or manual interaction, except for a basic cleaning, resulting in a high degree of automation. IBA reveals the potential resource value of the investigated granite and its local distribution showing potential extraction routes through the identification of the present phases.

Elemental compositions are highly important in many modern fields. In leaching of ores, the resulting leached sample and the missing elements would become visible on a grain/phase resolved scale, in contrast to a global view provided by dissolving methods. The elemental composition represents the state-of-charge of a battery cell, which it can locally measure without measuring a voltage. Processes in biology and pharmacology rely on the μm-resolved distribution of elements. Surface engineering requires minimal detection limits for coating development and quality control. Material development can be accelerated using the additional information revealed by IBA, accelerating finding solutions for climate change and the energy transition. Consequently, this work is the starting point for extending the use of IBA in industry, quality control, and research.

The technological advances of the last years yield major benefits in terms of accuracy, throughput, sample size, and versatility of IBA. Beyond state-of-the-art methods such as μ-PIXE, EDX or XRF it enables a full stoichiometric characterisation including trace quantities such as the detected Sr and light elements such as O, Li and B. The applied discrete mapping with fixed beam together with a full fitting of all spectra for each pixel represents a universal approach suitable for all lateral and sample scales, unifying former individual solutions for each length scale. The investigated scale is only a matter of the manipulator travel range, giving access to all spatial scales within a single device. This unification opens up a wide range of IBA applications in science and industry, similar to the widespread use of electron and x-ray microscopy. Further developments will allow for another 100-fold increase of the detector throughput via multi-detector setups and ASICs for RBS, NRA, and PIGE (PIXE SDDs already use ASICs), opening the path towards Megapixel tomographic IBA within this decade.

CRediT authorship contribution statement

S. Möller: Writing – review & editing, Writing – original draft, Visualization, Validation, Software, Project administration, Methodology, Investigation, Formal analysis, Data curation, Conceptualization. **K.F. Muzakka:** Software, Formal analysis. **D. Höschen:** Methodology. **M. Finsterbusch:** Supervision, Resources, Project administration, Funding acquisition.

Declaration of competing interest

The authors declare the following financial interests/personal relationships which may be considered as potential competing interests: Soeren Moeller reports a relationship with Aachen Ion Beams UG that includes: board membership and equity or stocks. Daniel Hoeschen reports a relationship with Aachen Ion Beams UG that includes: board membership and equity or stocks. If there are other authors, they declare that they have no known competing financial interests or personal relationships that could have appeared to influence the work reported in this paper.

Acknowledgments

This research was funded by the Federal Ministry of Education and Research (BMBF) within the project "For-Analytik" (grant number 13XP0445).

Data availability

Data available at DOI 10.5281/zenodo.13944189

References

[1] A. Merchant, S. Batzner, S.S. Schoenholz, M. Aykol, G. Cheon, E.D. Cubuk, Scaling deep learning for materials discovery, Nature (2023) 1–6, https://doi.org/10.1038/s41586-023-06735-9.
[2] C. Jeynes, et al., "Total IBA" – Where are we? *Nucl. Instrum. Methods Phys. Res., Sect. B* 271 (2012) 107–118, https://doi.org/10.1016/j.nimb.2011.09.020.
[3] S. Möller, Accelerator Technology: Applications in Science, Medicine, and Industry, in: Particle Acceleration and Detection, Springer International Publishing, 2020, https://doi.org/10.1007/978-3-030-62308-1.
[4] S. Möller, et al., A new high-throughput focused mev ion-beam analysis setup, Instruments 5 (1) (2021), https://doi.org/10.3390/instruments5010010.
[5] C. Jeynes, N.P. Barradas, E. Szilágyi, Accurate Determination of Quantity of Material in Thin Films by Rutherford Backscattering Spectrometry, *Anal. Chem.* 84 (14) (2012) 6061–6069, https://doi.org/10.1021/ac300904c.
[6] J.L. Colaux, C. Jeynes, K.C. Heasman, R.M. Gwilliam, Certified ion implantation fluence by high accuracy RBS, *Analyst* 140 (9) (2015) 3251–3261, https://doi.org/10.1039/C4AN02316A.
[7] G.W. Grime, F. Watt, Nuclear muscopy — Elemental mapping using high-energy ion beam techniques, *Nucl. Instrum. Methods Phys. Res., Sect. B* 50 (1) (1990) 197–207, https://doi.org/10.1016/0168-583X(90)90355-X.

[8] T. Calligaro, Y. Coquinot, L. Pichon, B. Moignard, Advances in elemental imaging of rocks using the AGLAE external microbeam, *Nucl. Instrum. Methods Phys. Res., Sect. B* 269 (20) (2011) 2364–2372, https://doi.org/10.1016/j.nimb.2011.02.074.
[9] T.F. Silva, et al., Elemental mapping of large samples by external ion beam analysis with sub-millimeter resolution and its applications, *Nucl. Instrum. Methods Phys. Res., Sect. B* 422 (2018) 68–77, https://doi.org/10.1016/j.nimb.2018.03.006.
[10] M. Mayer, 'SIMNRA User's Guide', p. 67, 1997.
[11] C. Jeynes, et al., Elemental thin film depth profiles by ion beam analysis using simulated annealing - a new tool, *J. Phys. d: Appl. Phys.* 36 (7) (2003) R97, https://doi.org/10.1088/0022-3727/36/7/201.
[12] M. Mayer, et al., Ion beam analysis of fusion plasma-facing materials and components: facilities and research challenges, *Nucl. Fusion* 60 (2) (Dec. 2019) 025001, https://doi.org/10.1088/1741-4326/ab5817.
[13] K.F. Muzakka, et al., Analysis of Rutherford backscattering spectra with CNN-GRU mixture density network, *Sci Rep* 14 (1) (2024) 16983, https://doi.org/10.1038/s41598-024-67629-y.
[14] R. da S. Guimarães, et al., Processing of massive Rutherford Back-scattering Spectrometry data by artificial neural networks, Nuclear Instruments and Methods in Physics Research Section B: Beam Interactions with Materials and Atoms 493 (2021) 28–34, https://doi.org/10.1016/j.nimb.2021.02.010.
[15] J. Demeulemeester, et al., Artificial neural networks for instantaneous analysis of real-time Rutherford backscattering spectra, *Nucl. Instrum. Methods Phys. Res., Sect. B* 268 (10) (2010) 1676–1681, https://doi.org/10.1016/j.nimb.2010.02.127.
[16] V.G. Oliveira, T.F. Silva, What do artificial neural networks learn? A study for analysis of RBS spectra, J. Phys.: Conf. Ser. 2340 (1) (2022) 012003, https://doi.org/10.1088/1742-6596/2340/1/012003.
[17] N.P. Barradas, A. Vieira, Artificial neural network algorithm for analysis of Rutherford backscattering data, PhysRevE 62 (4) (Oct. 2000) 5818–5829, https://doi.org/10.1103/PhysRevE.62.5818.
[18] L. Pichon, L. Beck, Ph. Walter, B. Moignard, T. Guillou, A new mapping acquisition and processing system for simultaneous PIXE-RBS analysis with external beam, *Nucl. Instrum. Methods Phys. Res., Sect. B* 268 (11) (2010) 2028–2033, https://doi.org/10.1016/j.nimb.2010.02.124.
[19] C. Jeynes, et al., External beam Total-IBA using DataFurnace, *Nucl. Instrum. Methods Phys. Res., Sect. B* 481 (2020) 47–61, https://doi.org/10.1016/j.nimb.2020.08.002.
[20] A. Tazzioli, Q. Lemasson, A. Girard, L. Pichon, B. Moignard, C. Pacheco, Advanced 2D-PIXE/RBS processing with Machine Learning at the New AGLAE facility for ancient layered objects, *Nucl. Instrum. Methods Phys. Res., Sect. B* 555 (2024) 165469, https://doi.org/10.1016/j.nimb.2024.165469.
[21] J.-C. Petit, G.D. Mea, Energetic ion beam analysis in the Earth sciences, Art. no. 6267, Nature 344 (6267) (1990), https://doi.org/10.1038/344621a0.
[22] C.G. Ryan, PIXE and the nuclear microprobe: Tools for quantitative imaging of complex natural materials, *Nucl. Instrum. Methods Phys. Res., Sect. B* 269 (20) (2011) 2151–2162, https://doi.org/10.1016/j.nimb.2011.02.046.
[23] J.L. Campbell, et al., The Guelph PIXE Software Package V, *Nucl. Instrum. Methods Phys. Res., Sect. B* 499 (2021) 77–88, https://doi.org/10.1016/j.nimb.2021.05.004.
[24] S. Möller, M. Finsterbusch, K.F. Muzakka, MeV Ion beam analysis of granite in 10000 points, Zenodo (2024), https://doi.org/10.5281/zenodo.13944189.
[25] S. Möller, R. Krug, R. Rayaprolu, B. Kuhn, E. Joußen, A. Kreter, Deuterium retention in tungsten and reduced activation steels after 3 MeV proton irradiation, Nuclear Materials and Energy (2020) 100742, https://doi.org/10.1016/j.nme.2020.100742.